

See discussions, stats, and author profiles for this publication at: <https://www.researchgate.net/publication/277086783>

Stable Iridium(IV) Complexes of an Oxidation-Resistant Pyridine-Alkoxide Ligand: Highly Divergent Redox Properties Depending on the Isomeric Form Adopted

ARTICLE in JOURNAL OF THE AMERICAN CHEMICAL SOCIETY · MAY 2015

Impact Factor: 12.11 · DOI: 10.1021/jacs.5b04185 · Source: PubMed

READS

41

6 AUTHORS, INCLUDING:



Dimitar Shopov

Yale University

5 PUBLICATIONS 68 CITATIONS

SEE PROFILE



Jesus Campos

University of Oxford

35 PUBLICATIONS 231 CITATIONS

SEE PROFILE



Robert Crabtree

Yale University

504 PUBLICATIONS 28,797 CITATIONS

SEE PROFILE

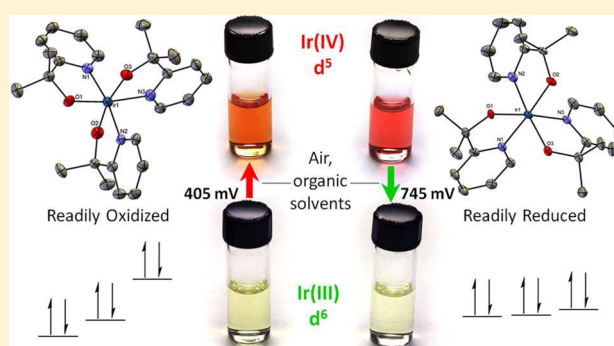
Stable Iridium(IV) Complexes of an Oxidation-Resistant Pyridine-Alkoxide Ligand: Highly Divergent Redox Properties Depending on the Isomeric Form Adopted

Dimitar Y. Shopov, Benjamin Rudsteyn, Jesús Campos,[†] Victor S. Batista,^{*} Robert H. Crabtree,^{*} and Gary W. Brudvig^{*}

Department of Chemistry, Yale University, New Haven, Connecticut 06520, United States

Supporting Information

ABSTRACT: The preparation of the facial and meridional isomers of $[\text{Ir}(\text{pyalk})_3]$ ($\text{pyalk} = 2\text{-(2-pyridyl)isopropanoate}$), as model complexes for a powerful water oxidation catalyst, is reported. The strongly donating N_3O_3 ligand set is very oxidation-resistant, yet promotes facile metal-centered oxidation to form stable Ir(IV) compounds. The $\text{Ir}^{\text{III/IV}}$ reduction potentials of the two isomers differ by 340 mV despite the identical ligand set. A ligand field rationalization is advanced and supported by DFT calculations.



INTRODUCTION

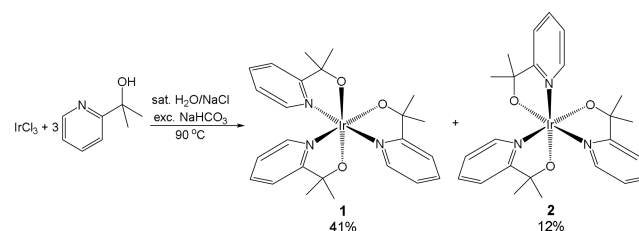
While reductive or reduced-state catalysis has long been a central theme of modern coordination chemistry, recent attention has begun to turn to oxidative processes.¹ Most notable of these is catalytic water oxidation for solar fuel production.² One of the biggest obstacles for designing appropriate homogeneous catalysts is the strong oxidizing conditions required to drive water oxidation. The majority of current ligands are unable to withstand such harsh conditions and decompose during the reaction.³ This is especially true for most electron-rich donor ligands, which are necessary for the stabilization of the high-valent metal centers involved in water oxidation. The development of ligands that combine powerful donicity with exceptional stability is essential for advancing the field.

High-valent iridium compounds illustrate the issue at hand. For example, the strong donor guanidinate ligands of Rohde and Lee⁴ give rise to iridium(IV) complexes with the lowest $\text{Ir}^{\text{III/IV}}$ redox potentials so far reported, but the ligands themselves also decompose at relatively mild potentials. On the other hand, robust polyaromatic ligands such as polypyridyls and phenylpyridyls are weaker donors yielding less accessible potentials (see Table 2 below). Additionally, cyclopentadienyl (Cp , Cp^*) ligands found to be extremely stable under most catalytic conditions were found to decompose readily when Cp^*Ir water oxidation precatalysts were exposed to oxidizing conditions.⁵

During our work with these same catalysts, we discovered that a particular supporting ligand exhibits extremely high stability under turnover conditions.⁶ This ligand, 2-(2-pyridyl)-isopropanol (Hpyalk), is a bidentate pyridine-alcohol chelator

which deprotonates to the propanoate (pyalk) upon coordination to even mildly electron-deficient metal centers. The ligand framework is highly resistant to oxidative degradation, having dimethyl-protected benzylic positions, while the tertiary alkoxide functions as a powerful electron donor. The combination of electron donation and oxidation resistance makes this ligand very suitable for stabilizing high metal oxidation states. Prior work has demonstrated that Ir catalysts bearing this ligand can withstand prolonged water oxidation without any sign of degradation.⁶ Unfortunately, our inability to obtain a single-crystal X-ray structure of our active catalyst limited the extent to which the properties of this ligand could be studied. To further this investigation using model complexes, we now report the two possible geometric isomers of $[\text{Ir}(\text{pyalk})_3]$: meridional isomer **1** and facial isomer **2** (Scheme 1). Both complexes were found to have stable Ir(III) and Ir(IV) states interchanging at easily accessible potentials.

Scheme 1. Formation of **1** and **2** with Isolated Yields



Received: April 22, 2015

Published: May 19, 2015

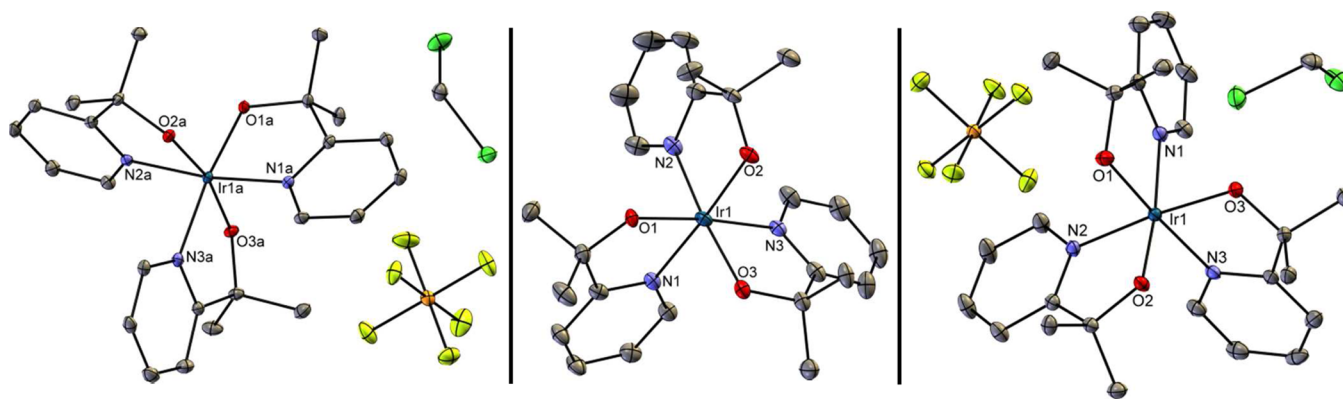


Figure 1. ORTEP crystal structures of $[1^{IV}]\text{PF}_6\cdot\text{CH}_2\text{Cl}_2$ (left), $[2^{III}]$ (middle), and $[2^{IV}]\text{PF}_6\cdot\text{CH}_2\text{Cl}_2$ (right) at the 30% probability level.

Interestingly, however, these potentials were found to be drastically different for each isomer. Ligand field theory and DFT calculations were employed to provide a rational explanation for these observations.

RESULTS AND DISCUSSION

Preparation and Initial Observations. Compounds **1** and **2** were found to form concurrently in various reactions between chloride salts of iridium, excess **Hpyalk**, and a weak base. While we report one of these procedures (using IrCl_3 in aqueous NaCl), the products also formed in various amounts when starting from hexachloroiridate salts or using a polar organic solvent such as acetone. Crude reaction products include 1^{III} partially oxidized to 1^{IV} by air, 2^{III} , and unidentified blue, slowly precipitating species, presumably iridium oxide nanoparticles from the basic hydrolysis of the starting Ir salts. In all observed reactions, complex **1** was more abundant than **2**, but both were always present. As both compounds in either oxidation state were found to stick to chromatography silica gel, separation was achieved by cation exchange chromatography after the mixture was selectively oxidized to cationic 1^{IV} and neutral 2^{III} . After subsequent oxidation, reduction, or neither, both isomers could be isolated as racemic mixtures of neutral yellow Ir(III) complexes or as deeply colored cationic Ir(IV) salts (orange for **1** and red for **2**), undergoing reversible one-electron conversion with a variety of oxidants and reductants such as sodium periodate and sodium ascorbate. However, the redox properties of **1** and **2** differ significantly: unlike **2**, reduced **1** is oxidized to Ir(IV) by air, whereas unlike **1**, oxidized **2** reacts with common organic solvents which are not readily oxidized, such as dichloromethane, acetone, and ethyl acetate, to become reduced to the Ir(III) state, even in the presence of air (both processes occur slowly, over the course of hours to days). Furthermore, weak oxidants such as ferrocenium or ferricyanide salts selectively oxidize **1** but not **2**. Both **1** and **2** are very stable in the presence of harsh oxidants such as periodates, chlorine, and air, even at elevated temperatures. Extensive decomposition has so far only been observed on heating the dry solids beyond 130°C in air. The complexes are also highly inert: Heating 2^{III} to 90°C in water for 5 days resulted in a roughly 25% conversion to **1**, while no conversion was observed from 1^{III} or 1^{IV} to **2**. These results indicate that the meridional geometry (**1**) is thermodynamically preferred.

Characterization. NMR data (both ^1H and ^{13}C) show one set of ligand peaks for 2^{III} , as expected from its C_3 symmetry, and three (partially overlapping) sets for 1^{III} , which has no

overall symmetry despite the C_{2v} N_3O_3 atom arrangement. Species $[1^{IV}]^+$ and $[2^{IV}]^+$ gave broad (0.5–4 ppm wide) proton signals in the range of -5 to 40 ppm, as expected for paramagnetic species. UV–visible absorption spectra of the two compounds in the Ir(IV) state (see Figure S1 in the Supporting Information (SI)) show absorption bands in the visible range with molar absorptivity on the order of $1000\text{ M}^{-1}\text{ cm}^{-1}$. These are consistent with the ligand-to-metal charge transfer bands observed in essentially all Ir(IV) compounds.

Crystal structures (Figure 1) were obtained for $[1^{IV}]\text{PF}_6$, $[2^{IV}]\text{PF}_6$, and 2^{III} , the last of which was unexpectedly found as an adduct with one $[\text{Mg}(\text{H}_2\text{O})_6]\text{Cl}_2$ unit per racemic pair of 2^{III} molecules. The structure indicates hydrogen bonding between the Ir alkoxo and Mg aqua ligands, taking full advantage of the favorable facial geometry (Figure S5). Intraligand bond lengths and angles (SI section VII) are similar for all structures and consistent with values from similar compounds. The effect of the oxidation state change is most noticeable in the Ir–O bond lengths, with a lesser impact on the Ir–N lengths (Table 1).

Table 1. Ir–L Bond Distances (Å) for **1** and **2** from Diffraction Data (bold), as well as from DFT Optimized Structures

bond	1^{III}	1^{IVa}	2^{IIIb}	2^{IVb}
Ir–N1	2.05	2.030; 2.07	2.029; 2.08	2.060; 2.10
Ir–N2	2.05	2.038; 2.06	2.016; 2.08	2.046; 2.09
Ir–N3	2.07	2.068; 2.12	2.032; 2.08	2.061; 2.13
Ir–O1	2.05	1.934; 1.95	2.041; 2.05	1.963; 1.95
Ir–O2	2.08	1.951; 1.98	2.038; 2.05	1.951; 2.01
Ir–O3	2.10	1.990; 1.98	2.040; 2.05	1.959; 1.97
RMSD ^c		0.05	0.12	0.10

^aCrystal data average for the two molecules in the asymmetric unit.

^bSymmetrically degenerate ligands; DFT and crystallographic values are paired arbitrarily. ^cRoot mean square positional deviation for inner-sphere atoms (IrN_3O_3).

The change in Ir–O lengths can be attributed to electrostatic and π -bonding interactions between the highly electron-donating alkoxo groups and the varying (between III and IV) electron-poor Ir center. Both the unvarying intraligand and varying ligand–metal bonds support a metal-centered redox process. DFT-optimized structures (see later discussion and Experimental Methods section) of both isomers in each oxidation state are in good agreement with the crystallographic data and demonstrate the expected trend in bond lengths.

Electrochemistry. Our initial redox observations of **1** and **2** prompted us to further investigate the complexes electrochemically. Cyclic voltammetry of the isomers in a pH 7.0 aqueous solution shows a reversible redox feature at 426 mV for **1** and 799 mV for **2** (vs NHE). Based on the characterizations and qualitative observations described above, we attribute this feature to the Ir^{III/IV} transition. Since the alkoxo groups can potentially protonate, pH effects were studied. Figure 2 shows

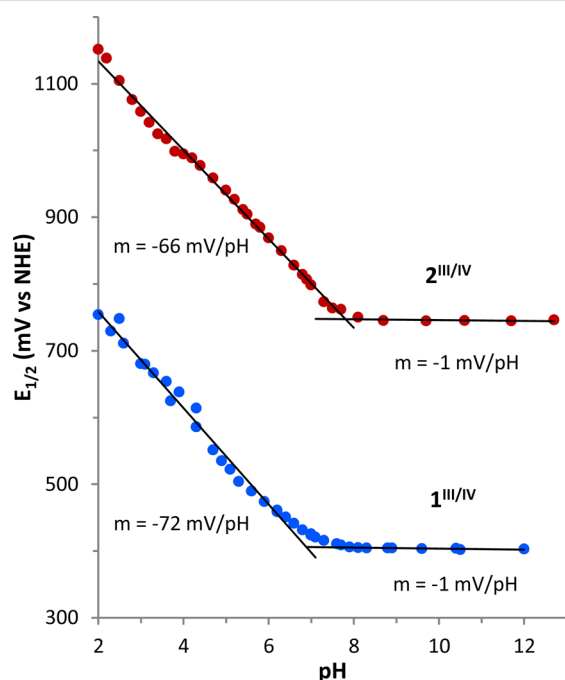


Figure 2. pH dependence of the electrochemical redox couples observed for **1** (blue) and **2** (red). Linear regression line fits and their slopes are given for data points below pH 6.8 (left) and above pH 8 (right).

the pH-dependent reduction potentials for the two complexes. Both exhibit similar behaviors, with proton coupling evident below pH 7 and no such effect above pH 8. As the latter trend extends invariantly into the strongly basic range, we assign it to transitions between fully deprotonated Ir^{III}/Ir^{IV} species for both isomers and will use the corresponding potentials (405 and 745 mV for **1** and **2**, respectively; Table 2) for further comparisons. The acidic trend, on the other hand, indicates proton loss on oxidation, implying that the alkoxo groups are weakly basic in the Ir(III) state. The lack of return to a flat slope at even lower pH implies that the Ir(IV) state has no significantly basic groups, as expected from the increased Lewis acidity. These results highlight the potential of **pyalk** to facilitate proton-coupled electron-transfer (PCET) processes under suitable conditions.

Interestingly, however, the slope of the acidic trend deviates noticeably from integral proton transfer (59 mV per (protons per electron) per pH unit), particularly for **1**. Since each complex has three basic alkoxo groups in fairly close proximity, it is likely that there are more complex interactions with protons, water molecules, or the electrolyte ions. We attempted to explore such interactions by adding various amounts of Mg²⁺ ions or increasing the electrolyte concentration. However, the potential shifts observed were too small to make any meaningful statements, aside from a noticeable potential drop in the case of **2** upon addition of as little as half an equivalent of

Table 2. Ir^{III/IV} Reduction Potentials for Various Octahedral Complexes with LX-Type Ligands as well as Cl[−]

ligand set	solvent	$E_{1/2}^a$ mer/other	$E_{1/2}^a$ fac
6(Cl [−])	water	0.91 ^c	
3(pyalk)	water	0.405	0.745
—	CH ₂ Cl ₂	0.194	0.528
3(picolinate)	MeCN	1.37 ^{b,d}	
3(2-phenylpyridine)	DMF	0.95 ^e	1.01 ^e
3(2-(<i>p</i> -tolyl)pyridine)	DMF	0.88 ^e	1.00 ^e
3(2-(4,6-difluorophenyl)pyridyl)	DMF	1.39 ^e	1.48 ^e
3(1-phenylpyrazolyl)	DMF	0.98 ^e	1.09 ^e
3(1-(4,6-difluorophenyl)pyrazolyl)	DMF	1.42 ^e	1.50 ^e
3(1-(4-trifluoromethylphenyl)pyrazolyl)	DMF	1.32 ^e	1.43 ^e
3(PhNC(NMe ₂)NPh [−])	CH ₂ Cl ₂	0.43 ^f	
3(PhNC(NEt ₂)NPh [−])	CH ₂ Cl ₂	0.37 ^f	
3(<i>p</i> -tol)NC(NMe ₂)N(<i>p</i> -tol) [−]	CH ₂ Cl ₂	0.29 ^f	

^aReported values in V converted to the NHE reference. Reduction potentials for FeCp₂⁺/FeCp₂ in organic solvents were taken from ref 10. ^bIrreversible oxidation. ^cReference 7. ^dReference 8. ^eReference 9. ^fReference 4.

Mg²⁺ (see Table S1). This likely results from the strong hydrogen-bonding interaction between the two metal complexes witnessed in the crystal structure of **2**^{III}.

Reduction potentials for the Ir^{III/IV} transition were also measured in dichloromethane and referenced against ferrocene. The results, −510 mV for **1** and −176 mV for **2** (194 and 528 mV vs NHE, respectively), are notably lower than the aqueous potentials, by about 215 mV. The relative difference between the two isomers, however, remains essentially unchanged (340 mV in water versus 334 mV in dichloromethane). A probable cause of this solvent shift is the hydrogen bonding of water. Both of the Pourbaix diagrams of Figure 2 and the crystal structure of **2**^{III} (refer to Figure S5) strongly indicate that the alkoxide groups are considerably basic and form strong hydrogen bonds with water molecules in the Ir(III) state. The overall effect of the latter is to withdraw excess ligand-sphere electron density away from the metal center, thus weakening the ability of the alkoxides to stabilize high-valent states. Since hydrogen bonding involves neutral water molecules, its influence is distinct from that of ligand protonation and is expected to be mostly pH-independent.

There are two interesting features about our reduction potentials. First, they are among the lowest Ir^{III/IV} couples ever observed, particularly in the case of **1**. While the aqueous potentials are very low, the dichloromethane ones are exceptional. For comparison, the most typical Ir(IV) species, hexachloroiridate, reduces at 910 mV in water. Redox values for some [Ir(LX)₃] complexes are given in Table 2. For this coordination motif, the guanidinate complexes of Rohde and Lee⁴ have a comparable Ir^{III/IV} transition, but we have found no reports of potentials lower than that of **1** in dichloromethane. Curiously, the related and more commonly used ligand picolinate does not seem to appreciably stabilize Ir(IV), instead irreversibly oxidizing at 1.37 V, according to Basu et al.⁸ The phenylpyridine family of ligands investigated by Tamayo et al.⁹ have an observable Ir(IV) state, but at significantly higher potentials.

The second point of interest is the great 330–340 mV disparity in the Ir^{III/IV} potential between **1** and **2**. Such a large effect is striking because the only difference between the two

compounds is the *fac/mer* orientation of the ligands (a difference consisting of a single ligand flip). The Tamayo study presents the only other reduction potential comparisons between facial and meridional isomers of $[\text{Ir}(\text{LX})_3]$ complexes. The reported *mer-fac* differences are significantly lower, but in all cases Ir(IV) is favored in the meridional geometry. This trend can be explained with ligand field theory. The Ir^{III} and Ir^{IV} states exist in octahedral, low-spin, d^6 and d^5 states, respectively. Facial complex **2** has 3-fold symmetry which puts the three t_{2g} orbitals in identical ligand fields, making them degenerate. On the other hand, meridional complex **1** has the high-field alkoxide groups arranged in a plane. This results in the splitting of t_{2g} orbitals and thus in a HOMO of higher energy. As a result, **1**^{III} can lose an electron more readily than **2**^{III}. In the resulting d^5 Ir(IV) state, ligand field repulsion is also more efficiently managed in **1**, as most of it is focused on the half-filled orbital.

The effects that ligands exert on the electronic properties of complexes have been the focus of numerous classical parametrization methods,¹¹ with the electrochemical scheme of Lever^{11a} being most relevant here. Lever's parameters were designed to predict the potential of redox transitions based on the net cumulative effect of all ligand arms around a metal; they do not account for isomer differences. In most cases, this appears to be a satisfactory model, as isomer effects are generally small. Lever notes, however, that strong acceptor ligands, in particular carbonyl and isonitriles, can impart greater redox differences based on relative orientation. This electronic argument, that strong acceptors lower the energies of coplanar t_{2g} orbitals, is inversely analogous to ours. Lever limits the discussion to acceptor ligands; we have shown here that isomer effects are also applicable to strong donors such as alkoxides and phenyls (it is possible that the effect is greater for iridium than ruthenium, the metal most studied by Lever, due to the stronger metal–ligand interactions of the former). Combining these observations, we can state that this effect is the result not of a particular ligand type, but of the *difference* in donor strengths between different types of coordinating groups.

Computational Studies. Redox and Thermodynamic Properties. In order to investigate these interesting properties of the two complexes in more detail, we used DFT to compute their energies and structures. We find that the ligand field explanation for the drastically different redox behaviors of the two isomers is consistent with calculated electronic structures. As expected, the three t_{2g} valence orbitals of **1**^{III} are significantly separated by about 0.5 eV, while those of **2**^{III} are nearly degenerate and display significant mixing (Figure 3). The elevation of the HOMO in meridional isomer **1**^{III} is quite prominent, and as expected, the orbital is aligned with the alkoxide-heavy plane. The quantitative results of the computation (Tables 3–5) are in good agreement with measurements. The difference in reduced-state HOMO energies (0.43 V) is similar to the measured redox difference. As for a more thorough treatment, taking the isomer-redox cross-difference of the total free energies of the four species yields an almost identical result (0.41 V), supporting the validity of pinning the isomer effect on HOMO energy differences. Further treatment using calculations of the reduction potential differences in implicit dielectric continuum solvent environments (see the Experimental and Computational Methods section) yields similar results. In fact, all of the above computational approaches actually overestimate the difference by a relatively small amount, 20–100 mV, which is

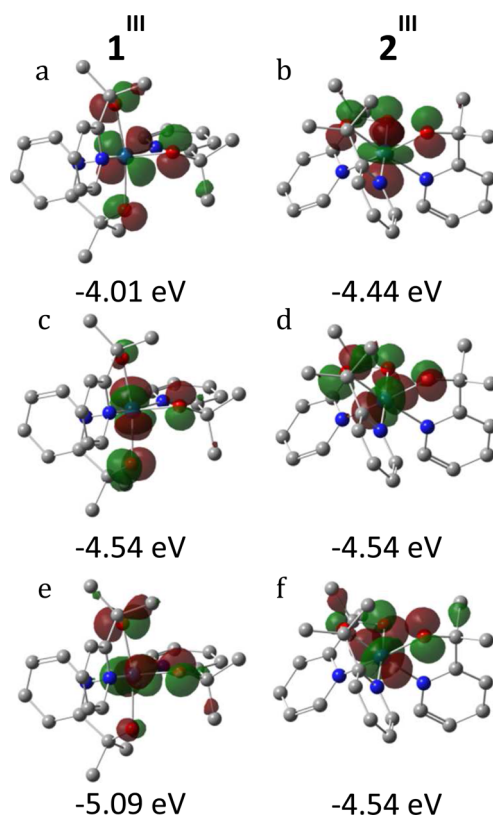


Figure 3. DFT-computed valence (t_{2g}) orbital energies and isosurfaces (isovalue 0.05) for **1**^{III} (a, c, e) and **2**^{III} (b, d, f), demonstrating the electronic impact of the isomerism. Hydrogens are omitted for clarity.

Table 3. Normalized Gas-Phase HOMO Density Distribution for the Ir, O, and N Atoms of **1^{III} and **2**^{III}, Calculated Using Atomic Orbital Coefficients**

atom	1 ^{III}	2 ^{III}
Ir	43.8%	47.0%
N1	0.19%	0.96%
N2	0.12%	0.96%
N3	0.82%	0.96%
O1	15.6%	10.6%
O2	12.4%	10.6%
O3	7.6%	10.6%

Table 4. Comparative Gas-Phase Energies from DFT Calculations

quantity	kcal/mol	volts
HOMO difference (1 ^{III} – 2 ^{III})	9.92	0.43
$\Delta G_{\text{reduced}}$ (1 ^{III} – 2 ^{III})	–13.43	
$\Delta G_{\text{oxidized}}$ (1 ^{IV} – 2 ^{IV})	–3.98	
ΔG_{redox} (1 ^{III} – 2 ^{III}) – (1 ^{IV} – 2 ^{IV})	–9.45	–0.41

Table 5. Experimentally Measured $E_{1/2}$ and Computed Ir^{III/IV} Reduction Potentials E of **2^{III/IV} Relative to **1**^{III/IV} in Different Solvents**

solvent	E_{expt} (mV)	E_{theor} (mV)	error (mV)
CH ₂ Cl ₂	334	358	24
H ₂ O	340	437	93

surprising since the experimental value is very large to begin with. Since this isomer effect is prominently displayed in the

electronic calculations, it is quite unlikely that the observed differences are the result of other, nonelectronic, disparate isomer behaviors.

In addition to redox properties, the isomer free energy differences within each oxidation state carry information about the relative thermodynamics. For both oxidation states, **1** is predicted to be lower in energy than **2**. This supports the observed isomerization from **2** to **1**. Interestingly, this is the opposite of what is observed for the tris-phenylpyridine-type complexes from Table 2, for which the facial isomer is thermodynamically favored.⁹

Electronic Structure: Origin of Oxidation. While electrochemical measurements give quantitative information about the thermodynamics of redox processes, they do not indicate whether the observed oxidation is metal-centered or ligand-centered. The electronic structures from our DFT calculations help illustrate the details of this process. Specifically, of primary relevance are the energies and atomic distributions of the frontier valence orbitals in each oxidation state, as well as the spin density distributions for the oxidized states.

Analysis of the HOMO for **1**^{III} and **2**^{III} shows that the orbital is mainly localized on the Ir center and to a lesser, but still large, extent on the alkoxide groups (see Figure 3 and Table 3). The two isomers show similar patterns in atomic contributions to the HOMO. Both **1**^{III} and **2**^{III} show a contribution near 45% from Ir and around 33% from all alkoxide O atoms, and only less than 3% from the pyridyl N atoms, with the remainder on other ligand atoms. As for the oxidized states, the computed spin density distributions for **1**^{IV} and **2**^{IV} show a very similar trend. Approximately 50% of the spin density is on Ir and 47% on the alkoxide O atoms, with practically no spin density on the pyridyls (see Figure 4 and Table 6). Unlike in the symmetric Ir(III) state, however, the spin distribution on the geometrically equivalent O atoms of **2**^{III} is unequal, with one bearing far less spin density than the others. This spin distribution, along with the computed Ir–L bond lengths (Table 1), is in agreement with the weak Jahn–Teller effect expected for a low-spin d⁵ metal. However, this effect is too weak to discern in the experimental bond lengths, which are additionally impacted by anisotropic crystal packing influences. In the case of **1**^{IV}, it is essentially impossible to disentangle a Jahn–Teller effect from the Jahn–Teller-like ligand anisotropy.

Comparisons between the Ir(III) HOMO and the Ir(IV) SOMO shapes and distributions also help in determining the origin of oxidation. In the case of **1**, both orbitals are very similar, supporting the expectation that the oxidation originates from a metal-centered orbital and that these are the redox-active orbitals (Figures 3 and 5). For complex **2**, however, interpretation is complicated by the degeneracy of t_{2g} orbitals in a C₃-symmetric ligand environment. The Ir(III) orbitals are nearly equal in energy, meaning that the electron lost on oxidation may not be assignable to one particular orbital. In the Ir(IV) state, spin polarization effects appear to dominate the energy ordering and geometry of the t_{2g} states. The β spin states are all higher in energy than the α states, making the SOMO electron third-highest in energy (Table 7). In addition, individual orbitals are less evenly shared between the Ir and ligand atoms (Figure 5 and Figure S4 in SI section V). However, the unoccupied β SOMO level, representing the lost electron, is nonetheless quite similar to the orbitals of the Ir(III) state.

Overall, both calculated spin and HOMO distributions indicate that the oxidation is indeed primarily centered on the

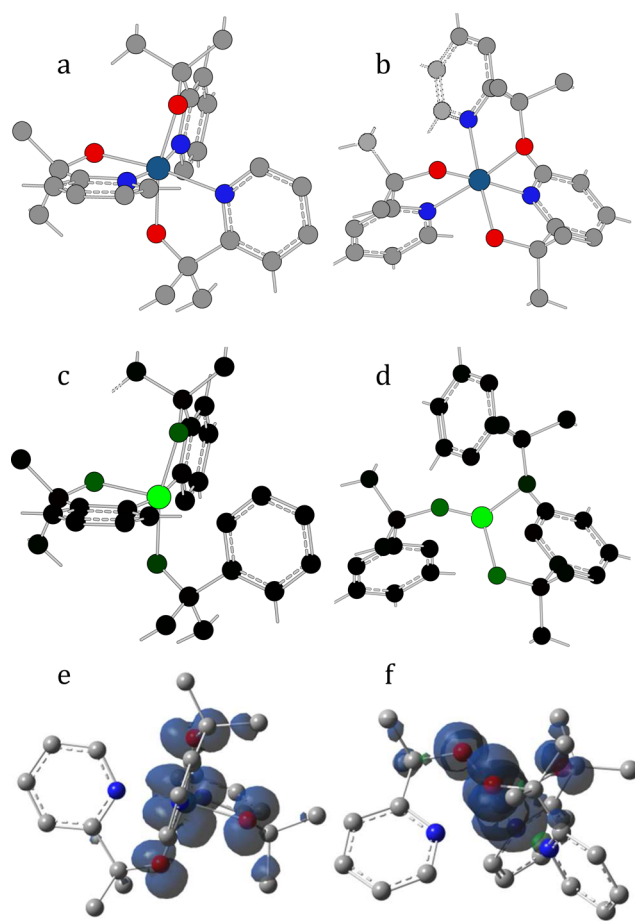


Figure 4. Gas-phase computed molecular geometries and Mulliken spin population for **1**^{IV} ((a) and (c), respectively) and **2**^{IV} ((b) and (d), respectively). Hydrogens are omitted for clarity. In panels (c) and (d), black represents a spin density of 0 while bright green represents high spin density (approximately 0.5). (e), (f): Spin density isosurfaces for **1**^{IV} and **2**^{IV}, respectively, calculated with an isovalue of 0.0015.

Table 6. Computed Gas-Phase Mulliken Spin Densities for the Ir, O, and N atoms of **1^{IV} and **2**^{IV}**

atom	1 ^{IV}	2 ^{IV}
Ir	0.51	0.48
N1	−0.01	0.00
N2	0.00	0.00
N3	0.00	−0.01
O1	0.18	0.21
O2	0.17	0.06
O3	0.12	0.21

Ir atom, with the highest molecular orbitals originating mostly from the t_{2g} orbitals of the metal. However, they also show that there is substantial delocalization on the alkoxide O atoms in both oxidation states (Figures 3, 5, and Figure S4 in SI section V). This demonstrates the capacity of the alkoxide groups to stabilize the radical character of Ir(IV) and points to a strongly covalent Ir–O bond. This is unexpected from the classification of Ir(IV) and alkoxide as “hard” coordination partners, which is generally associated with greater ionic bond character and illustrates the significance of secondary (π-bond) interactions.

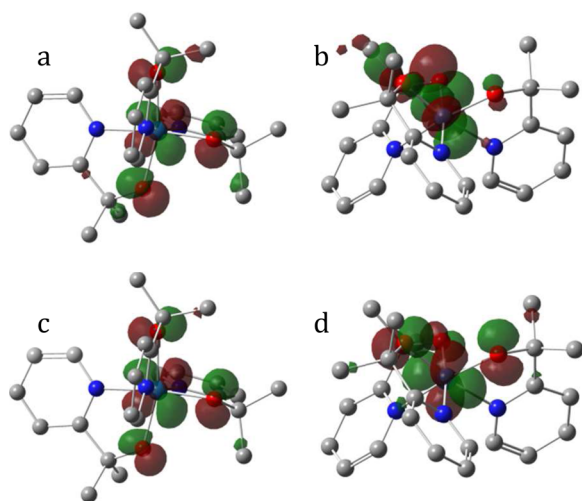


Figure 5. Isosurfaces (isovalue = 0.05) of the occupied SOMO(α) and unoccupied SOMO(β), for Ir^{IV} (panels (a) and (c), respectively) and Ir^{IV} (panels (b) and (d), respectively). Hydrogens are omitted for clarity. Isosurfaces for the remaining valence orbitals can be found in SI section V.

Table 7. Computed Gas-Phase Unrestricted MO Energies for the Valence Orbitals of Ir^{IV} and Ir^{IV} in eV^a

level	Ir^{IV}		Ir^{IV}	
	α	β	α	β
SOMO	−8.51	−6.05	−8.63	−6.47
HOMO−1	−9.05	−8.70	−8.94	−8.45
HOMO−2	−9.55	−9.15	−9.09	−8.62

^aLetters α and β denote electron spin. All levels besides SOMO(β) are occupied.

CONCLUSIONS

We have prepared and investigated reversibly oxidizable $\text{Ir}^{\text{III/IV}}$ complexes by employing an oxidation-resistant LX-type pyridine-alkoxide ligand. As an extremely strong donor, the alkoxide group favors high metal oxidation states while the large donicity difference between the two ligand arms leads to a dramatic influence on the $\text{Ir}^{\text{III/IV}}$ couple based on isomer geometry. A ligand field theory rationalization, supported by DFT calculations, accounts for the phenomenon in terms of differential distribution of the ligand field effects among the metal valence orbitals. We demonstrate that incorporation of alkoxide groups in ligand sets can stabilize high oxidation states, allowing for the isolation of species that would otherwise be transient or too unstable. In addition, it is made evident that ligand arrangement, not just ligand identity, needs to be taken into account when designing homogeneous catalysts, especially ones with highly disparate ligand types. This is particularly relevant for organometallic compounds, where it is not uncommon for ligands spanning the entire gamut of donicity to be found on the same metal atom.

EXPERIMENTAL AND COMPUTATIONAL METHODS

Physical Methods. *NMR Spectroscopy.* ^1H and proton-decoupled ^{13}C NMR spectra were collected on an Agilent Technologies DD2 600 MHz spectrometer equipped with a cold probe.

High-Resolution Mass Spectroscopy (HRMS). Mass spectra were taken on a 9.4 T Bruker Qe FT-ICR MS instrument in positive ion mode.

Electrochemistry. Cyclic voltammograms for the Pourbaix diagrams (Figure 2) were collected using a Princeton Applied Research VersaStat 4 potentiostat. Aqueous measurements were done with a boron-doped diamond working electrode, saturated aqueous Ag/AgCl reference electrode, and a platinum wire counter electrode. A scan rate of 100 mV/s was used. Solutions consisted of a pH 7.0 aqueous sodium phosphate buffer (0.2 M) and 2 mM analyte ($[\text{Ir}^{\text{IV}}]\text{PF}_6$ or 2^{III}). Adjustments to pH were made via addition of NaOH or H_2SO_4 and monitored using an electronic pH meter. Reported reduction potentials were referenced against a normal hydrogen electrode (NHE) potential using the standard accepted value of 0.197 V for saturated Ag/AgCl electrodes. Organic measurements were done in 0.1 M NBu_4PF_6 dichloromethane solution with a glassy carbon working electrode, platinum wire counter electrode, and a AgCl -coated silver wire pseudoreference electrode. Ferrocene was added to solutions as an internal reference. Compound $[\text{Ir}^{\text{IV}}]\text{PF}_6$ was used instead of 2^{III} due to excessive signal broadening with the latter, presumably caused by hydration of the compound due to its high polarity.

UV-visible Spectroscopy. Absorption spectra were collected using a Cary 50 spectrophotometer for solutions of 0.10 mM $[\text{Ir}^{\text{IV}}]\text{PF}_6$ or $[\text{Ir}^{\text{IV}}]\text{PF}_6$ in dichloromethane.

X-ray Crystallography. See SI section VII.

Computational Methods. All theoretical calculations were performed using the density functional theory (DFT) functional B3LYP¹² as implemented in Gaussian 09.¹³ The basis set consisted of LANL2DZ¹⁴ for Ir and 6-31G(d,p)^{15,16} for all other atoms. 590 angular points for each of the 99 radial shells were used in the integration grid. All oxidations were modeled as $\text{Ir}(\text{III})/\text{Ir}(\text{IV})$ with d^6/d^5 using the minimum energy structures. Redox potentials were computed using a Born–Haber cycle¹⁷ with gas-phase optimized structures used for both solvation steps as well as for the gas-phase ionization energy. Thermal corrections to free energy were computed using ideal-gas approximations as described by Cramer.¹⁸ The SMD implicit dielectric continuum solvation model¹⁹ was used to model dichloromethane ($\epsilon = 8.93$)¹³ and water ($\epsilon = 78.3553$).¹³ Molecular properties such as the spin density were computed in the gas phase.

Synthesis. General. Reagents and solvents were purchased from commercial sources and used as received without further purification. The ligand **Hpyalk** was prepared according to prior literature.²⁰ All other manipulations were carried out under ambient atmosphere.

Preparation (Mixed Isomers). To 190 mL of a saturated aqueous NaCl solution was added 1.40 g (4.0 mmol) of IrCl_3 hydrate, 1.64 g (12 mmol) of **Hpyalk** dissolved in 10 mL of water, and 1.01 g (12 mmol) of NaHCO_3 . The mixture dissolved fully as it was heated to 85 °C, at which temperature it was stirred for 22 h. The solution was cooled to room temperature, diluted with 200 mL of water, and oxidized with an excess (2.1 g, 10 mmol) of aqueous sodium periodate, NaIO_4 (rapid process). An excess (1.8 g, 10 mmol) of KPF_6 was added, and the desired products extracted with 6×100 mL portions of dichloromethane, until the aqueous layer appeared deep blue and the organic layer was nearly colorless. The organic extract evaporated under reduced pressure to a dark red-brown viscous residue. To remove excess free ligand, this was diluted with approximately 5 mL of dichloromethane and then partially precipitated with 10 mL of *n*-octane. The mixture was heated with manual stirring/grinding until the boiling point of *n*-octane was reached, while dichloromethane was allowed to evaporate. The viscous precipitate gradually solidified while being ground to a powder. The mixture was cooled, the solvent decanted, and the process repeated once more. The resulting brick-orange powder was dried under reduced pressure.

Separation and Isolation ($[\text{Ir}^{\text{IV}}]\text{PF}_6$ and 2^{III}). The above product was dissolved in 250 mL of water and reduced with an excess (1.2 g, 6 mmol) of sodium ascorbate (rapid process). The solution was saturated with NaCl , and the complexes were extracted using 6×25 mL portions of dichloromethane (until the aqueous layer became nearly colorless). After evaporation under reduced pressure, the

residue was again dissolved in 300 mL of water. Complex **1** was selectively oxidized by adding an excess (3.6 g, 11 mmol) of potassium ferricyanide, $K_3[Fe(CN)_6]$ (rapid process). The solution was once again saturated with NaCl, extracted with dichloromethane, and evaporated. The residue was then dissolved in water (approximately 300 mL) and flushed through a Biorex 70 cation exchange column (carboxylate type). Complex **2^{III}** eluted first as a yellow solution using pure water, while $[1^{IV}]^+$ was eluted subsequently as an orange band using a 0.1 M aqueous KPF_6 solution. Product $[1^{IV}]PF_6$ was isolated by extracting the orange fraction with dichloromethane (until the aqueous layer was colorless). Complex **2^{III}** was likewise isolated, with the additional prior step of saturating the aqueous solution with NaCl. The organic solutions were evaporated under reduced pressure to give brick-orange and yellow powders, respectively. Combined yield: 1.49 g, 53%.

mer-Tris(2-(pyridin-2-yl)propan-2-olato)iridium(IV) Hexafluorophosphate ($[1^{IV}]PF_6$). Yield from above preparation: 1.22 g, 41%.

Crystals suitable for X-ray crystallography were obtained by room temperature evaporation of a 1:1 dichloromethane/octane solution over 2 days. HRMS (FT-ICR): calcd for $[IrN_3O_3C_{24}H_{30}]^+$ (M^+): 601.1917 ($z = 1$). Found: $m/z = 601.1906$ ($z = 1$).

fac-Tris(2-(pyridin-2-yl)propan-2-olato)iridium(IV) Hexafluorophosphate ($[2^{IV}]PF_6$). An aliquot of **2^{III}** was readily oxidized to $[2^{IV}]PF_6$ by dissolving in water and oxidizing with an excess of $NaIO_4$, followed by addition of excess KPF_6 and extraction into dichloromethane (analogously to the manipulations described above), yielding a dark red residue on evaporation. Crystals suitable for X-ray crystallography were obtained by layering a dichloromethane solution with octane (approximately 1:2) and allowing undisturbed diffusion at $-20\text{ }^\circ\text{C}$ for 2 days. Room temperature crystallization fails, instead giving pale yellow crystals, as the complex is reduced by the solvent or impurities before crystals can form.

*mer-Tris(2-(pyridin-2-yl)propan-2-olato)iridium(III) (**1^{III}**)*. The compound is prepared by reducing an aliquot of $[1^{IV}]PF_6$ with an excess of sodium ascorbate, followed by extraction with dichloromethane and evaporation, yielding a yellow powder. Solutions become increasingly darker orange on exposure to air, converting to the Ir(IV) state over the course of days. 1H NMR (600 MHz, 0.1 M Na_2SO_3/D_2O): $\delta = 8.80$ (d, 1H, $^3J_{HH} = 6.4$ Hz, py), 8.79 (d, 1H, $^3J_{HH} = 6.0$ Hz, py), 7.75 (m, 3H, py), 7.58 (d, 1H, $^3J_{HH} = 5.7$ Hz, py), 7.34 (m, 3H, py), 7.22 (t, 1H, $^3J_{HH} = 6.7$ Hz, py), 7.20 (t, 1H, $^3J_{HH} = 6.7$ Hz, py), 7.05 (t, 1H, $^3J_{HH} = 6.7$ Hz, py), 1.68 (s 3H, Me), 1.67 (s 3H, Me), 1.56 (s 3H, Me), 1.54 (s 3H, Me), 1.51 (s 3H, Me), 0.94 (s 3H, Me). $^{13}C\{^1H\}$ NMR (150 MHz, 0.1 M Na_2SO_3/D_2O): $\delta = 178.3$, 177.3, 176.9 (py), 148.0, 147.7, 146.8 (py), 137.1, 137.0, 136.5 (py), 123.2, 122.9, 122.7, 122.4, 122.1, 122.0 (py), 83.9, 83.6, 83.4 (quat. C), 36.1, 35.0, 33.9, 33.8, 33.7, 32.9 (Me).

*fac-Tris(2-(pyridin-2-yl)propan-2-olato)iridium(III) (**2^{III}**)*. Yield from above preparation: 0.29 g, 12%.

Crystals suitable for X-ray crystallography were obtained from an alternate workup procedure otherwise identical to the one described above but with the additional steps of drying the organic portions postextraction using $MgSO_4$. The compound thus obtained was noticeably less soluble in dichloromethane, and crystals were grown by layering a 1:1 dichloromethane/acetone solution with hexane and allowing undisturbed diffusion. The complex was found to crystallize as an adduct, $[2^{III}]_2[Mg(H_2O)_6]Cl_2$, along with highly disordered solvent molecules. 1H NMR (600 MHz, 0.1 M Na_2SO_3/D_2O): $\delta = 7.84$ (t, 3H, $^3J_{HH} = 7.9$ Hz, py), 7.54 (d, 3H, $^3J_{HH} = 5.8$ Hz, py), 7.41 (d, 3H, $^3J_{HH} = 8.2$ Hz, py), 7.14 (t, 3H, $^3J_{HH} = 5.9$ Hz, py), 1.63 (s, 9H, Me), 1.21 (s, 9H, Me). $^{13}C\{^1H\}$ NMR (150 MHz, 0.1 M Na_2SO_3/D_2O): $\delta = 177.7$ (py), 148.2 (py), 137.2 (py), 124.2 (py), 123.1 (py), 83.6 (quat. C), 33.7 (Me), 33.4 (Me). HRMS (FT-ICR): calcd for $[IrN_3O_3C_{24}H_{31}]^+$ ($M + H^+$): 602.1989 ($z = 1$). Found: $m/z = 602.1976$ ($z = 1$).

■ ASSOCIATED CONTENT

Supporting Information

Structural data files and detailed crystallographic information, as well as additional experimental data are provided. The Supporting Information is available free of charge on the ACS Publications website at DOI: 10.1021/jacs.5b04185.

■ AUTHOR INFORMATION

Corresponding Authors

*victor.batista@yale.edu

*robert.crabtree@yale.edu

*gary.brudvig@yale.edu

Present Address

[†]Inorganic Chemistry Laboratory, Department of Chemistry, University of Oxford, South Parks Road, Oxford OX1 3QR, UK.

Notes

The authors declare no competing financial interest.

■ ACKNOWLEDGMENTS

This work was supported as part of the Argonne-Northwestern Solar Energy Research (ANSER) Center, an Energy Frontier Research Center funded by the U.S. Department of Energy, Office of Science, Office of Basic Energy Sciences, under Award Number DE-SC0001059. B.R. and V.S.B. acknowledge supercomputing time from NERSC and from the High Performance Computing facilities at Yale University.

■ REFERENCES

- (1) (a) Lyakin, O. Y.; Steinman, A. A. *Kinet. Catal.* **2012**, *53*, 738. (b) Freire, C.; Pereira, C.; Rebelo, S. *Catalysis*. **2012**, *24*, 116.
- (2) (a) Kärkäs, M. D.; Verho, O.; Johnston, E. V.; Åkermark, B. *Chem. Rev.* **2014**, *114*, 11863. (b) Parent, A. R.; Sakai, K. *ChemSusChem*. **2014**, *7*, 2070.
- (3) Crabtree, R. H. *J. Am. Chem. Soc.* **2014**, *136*, 174.
- (4) Rohde, J. U.; Lee, W. T. *J. Am. Chem. Soc.* **2009**, *131*, 9162.
- (5) (a) Blakemore, J. D.; Mara, M. W.; Kushner-Lenhoff, M. N.; Schley, N. D.; Konezny, S. J.; Rivalta, I.; Negre, C. F. A.; Snoeberger, R. C.; Kokhan, O.; Huang, J.; Stickrath, A.; Tran, L. A.; Parr, M. L.; Chen, L. X.; Tiede, D. M.; Batista, V. S.; Crabtree, R. H.; Brudvig, G. W. *Inorg. Chem.* **2013**, *52*, 1860. (b) Blakemore, J. D.; Schley, N. D.; Kushner; Lenhoff, M. N.; Winter, A. M.; D'Souza, F.; Crabtree, R. H.; Brudvig, G. W. *Inorg. Chem.* **2012**, *51*, 7749.
- (6) (a) Schley, N. D.; Blakemore, J. D.; Subbaiyan, N. K.; Incarvito, C. D.; D'Souza, F.; Crabtree, R. H.; Brudvig, G. W. *J. Am. Chem. Soc.* **2011**, *133*, 10473. (b) Hintermair, U.; Hashmi, S. M.; Elimelech, M.; Crabtree, R. H. *J. Am. Chem. Soc.* **2012**, *134*, 9785. (c) Hintermair, U.; Sheehan, S. W.; Parent, A. R.; Ess, D. H.; Richens, D. T.; Vaccaro, P. H.; Brudvig, G. W.; Crabtree, R. H. *J. Am. Chem. Soc.* **2013**, *135*, 10837. (d) Thomsen, J. M.; Sheehan, S. W.; Hashmi, S. M.; Campos, J.; Hintermair, U.; Crabtree, R. H.; Brudvig, G. W. *J. Am. Chem. Soc.* **2014**, *136*, 13826. (e) Sheehan, S. W.; Thomsen, J. M.; Hintermair, U.; Crabtree, R. H.; Brudvig, G. W.; Schmuttenmaer, C. A. *Nat. Comm.* **2015**, *6*, 6469. (f) Thomsen, J. M.; Huang, D. L.; Crabtree, R. H.; Brudvig, G. W. *Dalton Trans.* **2015**, in press. DOI: 10.1039/c5dt00863h.
- (7) Petrovic, S. *Chem. Educator* **2000**, *5*, 231.
- (8) Basu, S.; Peng, S. M.; Lee, G. H.; Bhattacharya, S. *Polyhedron* **2005**, *24*, 157.
- (9) Tamayo, A. B.; Alleyne, B. D.; Djurovich, P. I.; Lamansky, S.; Tsyba, I.; Ho, N. N.; Bau, R.; Thompson, M. E. *J. Am. Chem. Soc.* **2003**, *125*, 7377.
- (10) Connelly, N. G.; Geiger, W. E. *Chem. Rev.* **1996**, *96*, 877.
- (11) (a) Lever, A. B. P. *Inorg. Chem.* **1990**, *29*, 1271. (b) Tolman, C. A. *Chem. Rev.* **1977**, *77*, 313. (c) Perrin, L.; Clot, E.; Eisenstein, O.;

Loch, J.; Crabtree, R. H. *Inorg. Chem.* **2001**, *40*, 5806. (d) Masui, H.; Lever, A. B. P. *Inorg. Chem.* **1993**, *32*, 2199.

(12) Stephens, P. J.; Devlin, F. J.; Chabalowski, C. F.; Frisch, M. J. *J. Phys. Chem.* **1994**, *98*, 11623.

(13) Frisch, M. J.; Trucks, G. W.; Schlegel, H. B.; Scuseria, G. E.; Robb, M. A.; Cheeseman, J. R.; Scalmani, G.; Barone, V.; Mennucci, B.; Petersson, G. A.; Nakatsuji, H.; Caricato, M.; Li, X.; Hratchian, H. P.; Izmaylov, A. F.; Bloino, J.; Zheng, G.; Sonnenberg, J. L.; Hada, M.; Ehara, M.; Toyota, K.; Fukuda, R.; Hasegawa, J.; Ishida, M.; Nakajima, T.; Honda, Y.; Kitao, O.; Nakai, H.; Vreven, T.; Montgomery, J. A., Jr.; Peralta, J. E.; Ogliaro, F.; Bearpark, M.; Heyd, J. J.; Brothers, E.; Kudin, K. N.; Staroverov, V. N.; Kobayashi, R.; Normand, J.; Raghavachari, K.; Rendell, A.; Burant, J. C.; Iyengar, S. S.; Tomasi, J.; Cossi, M.; Rega, N.; Millam, N. J.; Klene, M.; Knox, J. E.; Cross, J. B.; Bakken, V.; Adamo, C.; Jaramillo, J.; Gomperts, R.; Stratmann, R. E.; Yazyev, O.; Austin, A. J.; Cammi, R.; Pomelli, C.; Ochterski, J. W.; Martin, R. L.; Morokuma, K.; Zakrzewski, V. G.; Voth, G. A.; Salvador, P.; Dannenberg, J. J.; Dapprich, S.; Daniels, A. D.; Farkas, Ö.; Foresman, J. B.; Ortiz, J. V.; Cioslowski, J.; Fox, D. J. *Gaussian 09*, R. D.; Gaussian, Inc.: Wallingford, CT, 2009.

(14) Hay, P. J.; Wadt, W. R. *J. Chem. Phys.* **1985**, *82*, 299.

(15) Hariharan, P. C.; Pople, J. A. *Theor. Chim. Acta.* **1973**, *28*, 213.

(16) Francl, M. M.; Pietro, W. J.; Hehre, W. J.; Binkley, J. S.; Gordon, M. S.; DeFrees, D. J.; Pople, J. A. *J. Chem. Phys.* **1982**, *77*, 3654.

(17) Konezny, S. J.; Doherty, M. D.; Luca, O. R.; Crabtree, R. H.; Soloveichik, G. L.; Batista, V. S. *J. Phys. Chem. C* **2012**, *116*, 6349.

(18) Cramer, C. J. *Essentials of Computational Chemistry: Theories and Models*, 2nd ed.; Wiley: 2004.

(19) Marenich, A. V.; Cramer, C. J.; Truhlar, D. G. *J. Phys. Chem. B* **2009**, *113*, 6378.

(20) Wong, Y.-L.; Yang, Q.; Zhou, Z.-Y.; Lee, H. K.; Mak, T. C. W.; Ng, D. K. P. *New J. Chem.* **2001**, *25*, 353.